

The Influence of Triaxial Halos on Collisionless Galactic Disks

Jeremy L. Tinker and Barbara S. Ryden

Department of Astronomy, Ohio State University,
140 W. 18th Avenue, Columbus, OH 43210, USA
E-mail: tinker, ryden@astronomy.ohio-state.edu

ABSTRACT

We investigate the effect of rotating, triaxial halos on disk galaxies through an extensive set of numerical N -body simulations. Our simulations use a rigid potential field for the halos and bulges and collisionless particles for the disks. The triaxiality and the rotation rate of the halo are varied, as well as the masses of all three galaxy components. We analyze both the bar stability and the spiral response of the disks under these conditions.

We characterize most of our models by the mass ratio of the disk to the halo at 2.3 disk scale lengths, $(M_d/M_h)_{R_\odot}$. For models with a mass ratio greater than 0.8, a halo pattern speed $\Omega_h = 6.7 \text{ km s}^{-1} \text{ kpc}^{-1}$, and a intermediate-to-major axis ratio $q_b = 0.85$, a strong bar will develop within 3 Gyr, even for models with a bulge mass $M_b = 0.3M_d$. Models in which the bulge mass is reduced by half develop bars earlier and with lower Ω_h .

We create an artificial Hubble sequence of disk galaxies by varying the bulge-to-disk ratio of our models from 0 to 2.5. The torque induced by a rotating, non-axisymmetric halo creates bisymmetric spiral structure in the disk. We find that the pitch angle of the spiral arms in these models follows the same general trend found in observations of spiral galaxies, namely that later type galaxies have higher pitch angles. Our simulations follow closely the observational relation of spiral pitch angle with maximum rotational velocity of the disk, where galaxies with faster rotation have more tightly wound spiral arms. This relation is followed in our simulations regardless of whether the dominating mass component of the galaxy is the disk, the halo, or the bulge.

Subject headings: galaxies: spiral – galaxies: stability – methods: numerical

1. Introduction

Galaxies are not spherical objects. Although it is difficult to measure the intrinsic shapes of astronomical bodies from their projected light distributions, inferences can be made from their observed ellipticities. Many studies of the distribution of observed axis ratios of galaxies and galaxy clusters (e.g. Ryden, 1992, 1996; Tremblay & Merritt 1996) have shown that they are well represented by a population of intrinsically triaxial objects. Similar statistical analysis performed

by Alam & Ryden (2002) with a much larger sample of galaxies from the Sloan Digital Sky Survey Early Data Release has strengthened the claim that the observed distributions of ellipticities cannot be fit by projections of oblate or prolate spheroids.

This type of analysis is only available in the cases where the mass distribution creates light. The shapes of dark matter halos, therefore, must be inferred from even more indirect means. Proxy measures of the shape of our own halo offer widely varying results. The tidal stream of the Sagittarius dwarf galaxy implies a nearly spherical halo (Ibata et al. 2001), in contrast to the results of star counts, which give a minor to major axis ratio of ~ 0.6 (Siegal et al. 2002). The dark matter halos created in numerical studies of structure formation are non-axisymmetric systems. N -body simulations of dissipationless collapse in the cold dark matter (CDM) scenario by Dubinski & Carlberg (1991) showed that the resulting virialized halos deviated substantially from spherical symmetry and from axisymmetry, with average axis ratios $\langle c/a \rangle = 0.5$ and $\langle b/a \rangle = 0.7$, where a , b and c are the major, intermediate, and minor axes respectively. Simulations of larger cosmological volumes, which more adequately reproduce the hierarchical nature of structure formation in CDM, have also shown that dark matter halos are triaxial (Barnes & Efstathiou 1987; Warren et al. 1992). Analysis of the currently favored Λ CDM cosmology has shown similar results (Jing & Suto 2002).

The simulations cited above consist only of a collisionless dark matter component and include no gas dynamics. The introduction of a gas and stellar disk in the equatorial plane of the halo would certainly have effects on the internal structure of the halo. Fully self-consistent cosmological simulations of dissipational structure formation have problems reproducing more than general galactic attributes (e.g. Murali et al. 2002), and the resulting halo shape has not been the focus of these efforts. However, Dubinski (1994) showed that the adiabatic growth of a disk-like potential in a triaxial halo did not influence $\langle c/a \rangle$, while the intermediate to major axis ratio was only slightly increased to $\langle b/a \rangle \gtrsim 0.7$.

Models and simulations of disk galaxies, however, usually employ spherical halos, which do not reflect these results from CDM simulations. The purpose of most current investigations of galaxy-scale simulations has been modeling transformations of galaxies through major mergers (e.g. Barnes 1992; Dubinski, Mihos, & Hernquist 1999), minor encounters (e.g. Struck 1997; Thakar & Ryden 1998) and gas-dynamical effects (e.g. Mihos & Hernquist 1996; Springel 2000). The triaxiality of the halo does not immediately effect the results of these simulations and the implications of using triaxial halos have not been explored.

Early studies of the stability of disk galaxies (e.g. Ostriker & Peebles 1973; Hohl 1976; Efstathiou et al. 1982) demonstrated that a cold, rotationally supported disk is dramatically unstable to bar formation. This fact was used as justification for the existence of heavy, spherical, dark matter halos enveloping disk galaxies. This dynamically hot component of the galaxy inhibits bar formation. It has also been shown that a dense core gives a galaxy an inner Lindblad resonance, which does not allow swing amplification of waves through the center of the galaxy

and thus acts as a bar suppressant (Sellwood 1989)¹. In all cases the stabilizing mass component has been assumed to have spherical symmetry. If these galaxies were enveloped by triaxial halos, they would be more susceptible to bar instabilities. A systematic exploration of the stability of disks with non-axisymmetric halos has not been conducted. Curir & Mazzei (1999) presented fully self-consistent gas-dynamical simulations of disk galaxies with triaxial halos, but only used two halo models and did not employ bulges. The resolution in their simulations was severely limited ($N_{disk} = 3,000$), far less than the number of particles used by Efstathiou et al. (1982) which Sellwood (1989) found to be insufficient.

The notion that the potential field of a galaxy may contain non-axisymmetric features is not a new one; it is, in fact, readily apparent from the bars seen in many galactic disks. The effect of an oval distortion, like a bar, on a gas disk has been proposed as a driving mechanism for spiral density waves (Lin 1970). This idea has been explored numerically as well (Sanders & Huntley 1976; Sanders 1977; Huntley et al. 1978). These early simulations generally were limited to two-dimensional, massless disks driven by an analytic distortion to the symmetric potential, but were successful in creating significant spiral response in the disk. However, bar forcing does not reproduce tightly bound spiral patterns. And in comparison to Sanders & Huntley (1976), the response of the outer disk is weak when a more realistic bar potential, one that drops off faster with radius, is used in the simulation (Sanders & Tubbs 1980). Observationally spiral patterns are as common in barred galaxies as galaxies without bars. Also, there is evidence that bars and spiral arms have different pattern speeds, showing that one feature may not drive the other (Sellwood & Sparke 1988). A triaxial halo would not be subject to these concerns since the potential of the dark matter would dominate the outer regions of the disk, especially low mass disks which are stable to bar formation.

The bulge-to-disk ratio of a spiral galaxy, as well as the tightness of the spiral pattern, are two integral criteria of the Hubble classification scheme. On the average, there exists a smooth increase in pitch angle with later Hubble types (Kennicutt 1981). Such a correlation, however, is little more than a consistency check between classification parameters, and there exists significant scatter in the measured pitch angle for a given Hubble type.

Even with this scatter, the correlation between arm pattern and galaxy type has prompted several theoretical studies on the origin of this relation (see Kennicutt & Hodge 1982, and references therein). Kennicutt (1981) found that the correlation between pitch angle and maximum rotational velocity of the disk was as good as the theoretical model predictions, suggesting that the mass distribution and its resulting rotation curve is an important determinant in producing the shape of spiral arms. A more massive or more concentrated bulge will induce higher rotation velocities and loosely follow the correlation with Hubble type as well.

¹Efstathiou et al. (1982) did perform two simulations with dense centers but found that it did not make their disks stable. Sellwood proposed that the low resolution of their simulations was responsible for the results of their “bulge” simulations.

Our simulations include a collisionless stellar disk and a stiff, rotating halo. Most simulations include a bulge, which is also stiff. Our use of dissipationless simulations with halos which are not fully self-consistent allows us to cover a significant range of parameter space for all three galaxy components; the disk, bulge, and halo.

The structure of this paper is as follows: §2 presents our initial conditions as well as the N -body techniques used in this study. §3 shows the analysis and results of our fiducial simulation. §4 describes our suite of different galaxy models. In §5 we investigate the stability of our models with different halo and bulge masses, as well as different halo rotation rates. §6 presents our results for the spiral morphology of our simulations. We present results for models which follow the bulge-to-disk ratios of the Hubble sequence and models which vary widely in rotation velocity. We compare our results to observations of spiral galaxies.

2. Numerical Methods

2.1. Initial Conditions

The positions and velocities of the disk particles are initialized in the method outlined by Hernquist (1993). The density distribution of the disk is described by

$$\rho(R, z) = \frac{M_d}{4\pi h^2 z_0} \exp\left(-\frac{R}{h}\right) \text{sech}^2\left(\frac{z}{z_0}\right) \quad (1)$$

where R and z are cylindrical coordinates, h and z_0 are the scale length and scale height of the disk, and M_d is the total mass of the disk. The circular velocity and velocity dispersions are obtained from

$$v_c = \sqrt{|a_R|R} \quad (2)$$

$$\sigma_R^2 = \sigma_{R,0}^2 \exp(-R/h) \quad (3)$$

$$\sigma_z^2 = \pi G \Sigma(R) z_0 \quad (4)$$

$$\sigma_\phi^2 = \sigma_R^2 \frac{\kappa^2}{4\Omega^2} \quad (5)$$

where a_R is radial acceleration, Σ is the surface density of the disk, κ is the epicyclic frequency and Ω is the angular rotation rate. The radial acceleration in equation (2) is the total acceleration contributed by the self-gravity of the disk, the dark matter halo, and a spherical bulge. The

normalization of the radial velocity dispersion, $\sigma_{R,0}^2$, is obtained by requiring σ_R at a specified radius R_0 to be a multiple of the critical dispersion at that radius:

$$\sigma_{R=R_0} = Q \frac{3.36 G \Sigma(R_0)}{\kappa(R_0)} \quad (6)$$

where Q is Toomre’s parameter for gravitational stability in a rotationally supported disk. The disk models in this paper are defined to have $Q = 1.5$ at $R = 2.43h$, which in the Milky Way galaxy would be approximately the solar radius. The rotational velocity of each particle is then given by

$$\overline{v_\phi}^2 - v_c^2 = \sigma_R^2 \left(1 - \frac{\kappa^2}{4\Omega^2} - 2\frac{R}{h} \right). \quad (7)$$

The different halo models used in this paper can be represented by Dehnen’s (1993) γ -models;

$$\rho(r) = M_h \frac{3-\gamma}{4\pi} \frac{r_0}{r^\gamma (r+r_0)^{4-\gamma}} \quad (8)$$

where γ is the interior logarithmic slope of the density profile and r_0 is the scale length of the halo. A model with $\gamma = 1$ corresponds to a model proposed by Hernquist (1990) for bulges and elliptical galaxies. A spherical Hernquist model is used here to represent the bulges of our galaxies. Dubinski & Carlberg (1991) showed that the Hernquist model is a good fit for CDM halos, and is close to the general density profile for dark halos found by Navarro, Frenk, & White (1997), which also asymptotes to $\sim r^{-1}$ at small radii. The γ -models can be generalized to triaxial systems by replacing the radial coordinate r with m , where

$$m^2 = \frac{x^2}{a^2} + \frac{y^2}{b^2} + \frac{z^2}{c^2} \quad (9)$$

where a , b , and c are once again the principal axes of the system.

In practice, the disk-particle positions are sampled from the density function in equation (1), the accelerations on each particle from the different galaxy components are computed, and then the velocity dispersions and the rotational velocity of each particle are calculated. The peculiar velocities of each particle are sampled from Gaussian probability distributions with dispersions given by equations (3)-(5). Because κ and Ω in equations (5)-(7) are assumed to be azimuthally symmetric, the velocities for the disk particles are computed assuming that the halo is spherical; therefore when the disk models are placed inside a triaxial halo they are initially out of equilibrium.

2.2. N-body Techniques

To compute the self-gravity of the disk particles, we have employed GADGET (Springel, Yoshida, & White 2001), a tree code based on the hierarchical algorithm of Barnes & Hut (1986). GADGET employs a spline-softened force calculation that is expanded to quadrupole order for particle-cell interactions. The timesteps are continuously varying and individual for each particle. The spatial and time resolutions are set by the smoothing length, ϵ , and the timestep accuracy parameter, α . For simulations with $N = 10^5$, which are the majority of the simulations in this paper, these parameters were set to $\epsilon = 0.057$ and $\alpha = 0.04$.

The gravitational contribution of the halo is computed by the self-consistent field (SCF) method of Hernquist & Ostriker (1992). This method is based on the expansion of the galaxy potential in an orthonormal set of basis functions. The accuracy of the potential calculated is driven by the number of terms in the expansion. The numbers n and l determine the number of radial and angular basis functions used. The integration time, however, is a linear function of the number of terms as well. We found that the best balance of accuracy and speed was achieved with $n=16$ and $l=10$, which were the values used in all the simulations. The zeroth-order basis function was chosen to be the Hernquist profile, and the coefficients of the expansion were computed by Monte Carlo sampling of the halo density distribution, $\rho(m)$. Since the coefficients only have to be calculated once for each halo model, accurate calculations can be made by initially sampling a large number of particles from each halo profile, $\sim 10^7$ particles. The SCF method has been used frequently to model triaxial systems (e.g. Merritt & Quinlan 1998; Holley-Bockelmann et al. 2001). When comparing the force on a set of test particles calculated from the SCF coefficients with the force calculated from direct summation over the particles used for the coefficients, the rms error was $\sim 6 \times 10^{-3}$. This error level was maintained in models where γ was not equal to unity.

The contribution to the potential of the galaxy from the bulge can be computed analytically. Therefore, the total acceleration of each particle is given by

$$\mathbf{a}_i = \mathbf{a}_{tree} - \frac{M_b}{(r + r_b)^2} \hat{\mathbf{r}} - \sum_{n,l,m} A_{nlm} \nabla \Phi_{nlm}. \quad (10)$$

The first term is the acceleration returned by GADGET from walking the tree of disk particles. The middle term is the acceleration from the bulge, with the subscript b denoting bulge properties. The third term in equation (10) is the acceleration computed from the SCF expansion of the halo potential. The particle timesteps are inversely proportional to the particle acceleration, $\Delta t_i = \alpha/|\mathbf{a}_i|$.

3. Simulating a Milky Way Galaxy

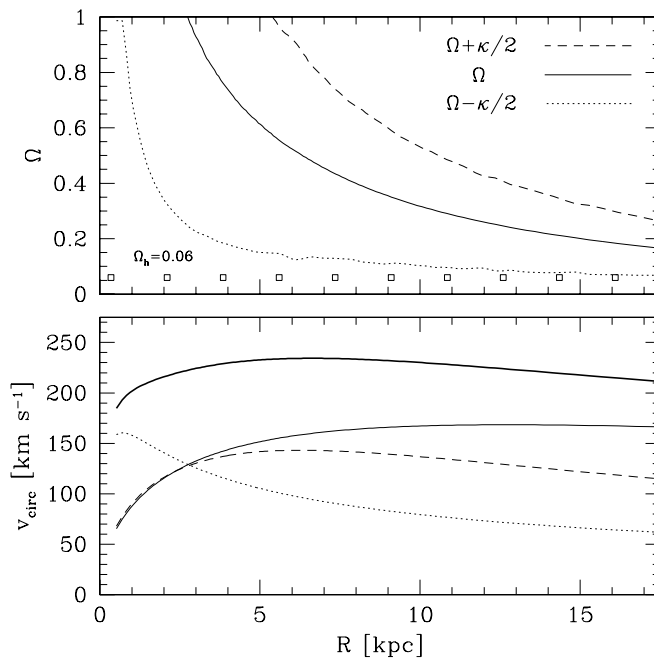


Fig. 1.— *Top Panel:* The Ω , $\Omega + \kappa/2$, and $\Omega - \kappa/2$ resonances are plotted against radius for the fiducial model. The square-dotted line at the bottom of this plot marks the halo rotation rate. This model has an inner Lindblad resonance near 15 kpc. *Bottom Panel:* The total circular velocity of the fiducial model is plotted with the thick solid line. The constituent parts of the galaxy are plotted with the dotted line (the bulge), the thin solid line (the halo), and the dashed line (the disk).

3.1. Parameters of the Fiducial Simulation

Table 1 lists the physical parameters of the fiducial simulation. Scaling our N -body units to physical values reasonable for the Milky Way galaxy as in Hernquist (1993), we get $h = 3.5$ kpc and $M_d = 5.6 \times 10^{10} M_\odot$, making the unit of time 13.1 Myr. With these scalings, the value of the rotational speed at the solar radius, $R_\odot = 2.43h$, is nearly 220 km s^{-1} . The fiducial halo rotation rate, $\Omega_h = 0.06$, is equivalent to a pattern speed of $4.5 \text{ km s}^{-1} \text{ kpc}^{-1}$ in these unit. (For comparison, the simulations of Bekki & Freeman (2002), in which a massless gas disk is embedded in a rotating triaxial halo, use a pattern speed of $3.8 \text{ km s}^{-1} \text{ kpc}^{-1}$.) Figure 1 shows the contributions of each galaxy component to the total circular velocity. Figure 1 also shows the values of the Ω , $\Omega + \kappa/2$, and $\Omega - \kappa/2$ resonances as a function of radius. Although the simulations of Dubinski (1994) suggest that the equatorial plane of the halo can be as elliptical as $b/a = q_b = 0.7$, we chose a more moderate value of $q_b = 0.85$ for our fiducial simulation. The minor axis ratio, $c/a = q_c$, was set to 0.7. Figure 2 plots the fractional difference in the potential along the x and y axes of halos with different values of q_b . The dotted line represents the asymmetry of the potential from the entire fiducial model. At five scale lengths, the difference in the halo potential is $\sim 3\%$, while the difference in the total system potential is $\sim 2\%$.

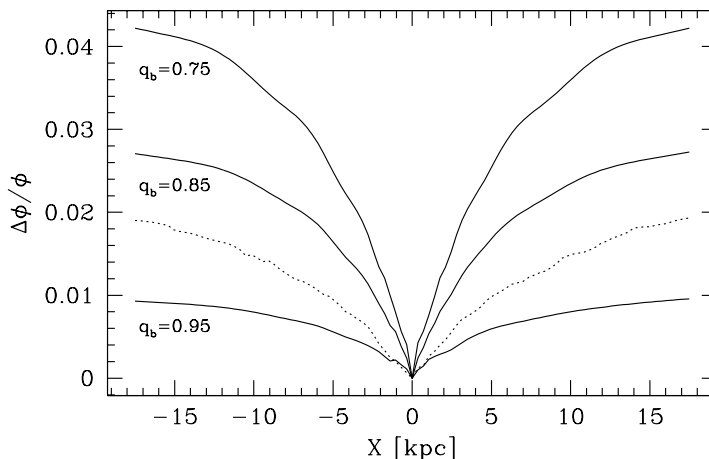


Fig. 2.— The fractional difference in the halo potential between the x and y axes is plotted against the x axis. The three solid lines show halos with different values of q_b . The dotted line plots the initial potential asymmetry of the entire fiducial model, disk, bulge and halo with $q_b = 0.85$.

To test our numerical method, we ran a simulation with a spherical halo but still computed the halo’s contribution to the potential through the SCF method. Outside of the shape of the halo, which was set to $q_b = q_c = 1$, all the parameters listed in Table 1 were the same. The simulation was run to a time of 500, which corresponds to a physical time of 6.55 Gyr. Figure 3 shows the rotation curve, the surface density, and the vertical particle density for the initial and final states of the simulation. These curves show remarkably little deviation from their initial values, proving that the integration of the SCF into GADGET works well for this type of simulation.

3.2. Analyzing the Simulations

The fiducial model was integrated to a time of 6.55 Gyr as well. The influence of the triaxial halo of the density structure and rotation curve can be seen in Figure 4. As in the simulation with the spherically symmetric halo, there is little change in the azimuthally averaged structure of the disk. The maximum of the rotation curve is slightly lower than the initial velocity, caused by a slight heating of the disk as rotational energy is transformed into thermal. It is interesting to note that the vertical structure of the disk does not change even after this lengthy integration time. The disk is not vertically heated by the constant perturbation of the halo potential.

Structure in the disk is generated by the influence of the halo. A time-varying, non-axisymmetric potential creates a torque on the disk, and it is expected that symmetric, $m=2$ structures should form. Figure 5 shows an image of the fiducial model at a time of 655 Myr. The bisymmetric structure is apparent. To quantify the response of the disk to the halo potential, we performed a Fourier decomposition of the surface density of the disk into logarithmic spirals (Sellwood & Athanassoula 1986; Binney & Tremaine 1987) of the form $\alpha u + m\phi = ct$, where

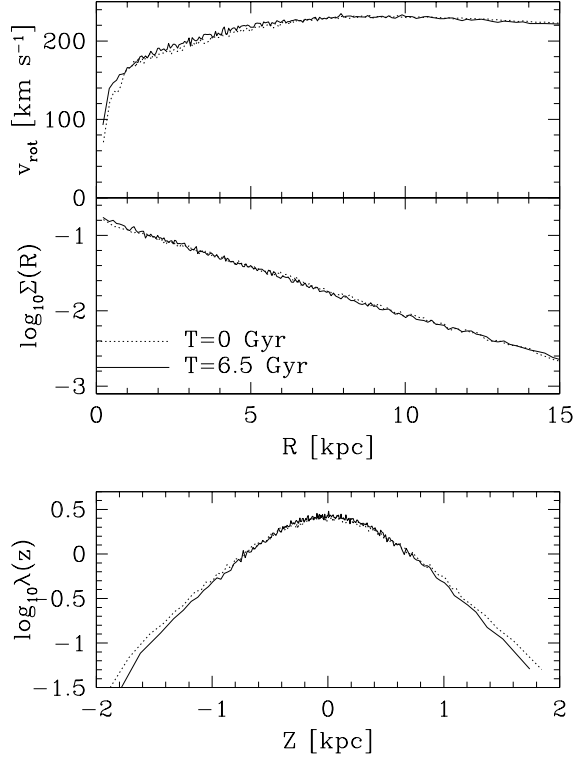


Fig. 3.— Properties of the initial (*dotted line*) and final states (*solid line*) of the spherical-halo model are plotted. The top two panels plot the rotational velocity and the surface density against cylindrical radius. These statistics were calculated by binning particles in cylindrical rings of varying width, but with 500 particles per bin. The bottom panel plots the vertical linear density λ against vertical height z . This was calculated by binning particles by the absolute value of their z -coordinate with 500 particles per bin.

$u = \ln R$ and ϕ is the azimuthal angle. The amplitude A of each Fourier component is the Fourier transform of the surface density $S(u, \phi)$;

$$A_m(\alpha) = \frac{1}{(2\pi)^2} \int_{-\infty}^{\infty} du \int_0^{2\pi} S(u, \phi) e^{i(\alpha u + m\phi)} d\phi. \quad (11)$$

In practice, since an N -body simulation is resolved by discrete particles, the integral signs can be replaced by a summation over all particles and equation (11) then becomes

$$A_m(\alpha) = \frac{1}{N} \sum_{j=1}^N e^{i(\alpha u_j + m\phi_j)}. \quad (12)$$

The parameter m was set to 2 to look for bisymmetric structure, and coefficients were calculated for values of $-25 \leq \alpha \leq 25$. The decomposition of the fiducial model at 655 Myr is shown in

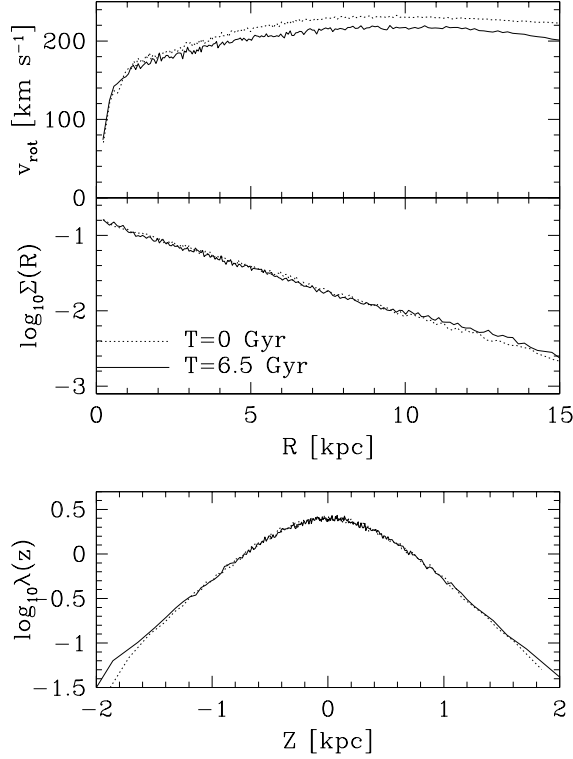


Fig. 4.— Same as Figure 3. The halo in this model is now triaxial, with $q_b = 0.85$ and $\Omega_h = 0.06$. There is little difference between the initial and final states of the simulation.

Figure 6. The decomposition of the model with the spherical halo at the same time interval is shown for comparison. Power at negative values of α corresponds to leading spiral waves. Power at positive values of α corresponds to trailing spiral waves, which in the fiducial model have a distinct peak at $\alpha = 12$. The pitch angle p for this logarithmic spiral can be calculated from $p = \tan^{-1}(m/\alpha) = 9.5^\circ$. Smaller values of α correspond to more loosely-bound spiral patterns, or arms with a larger pitch angle. The peak seen in Figure 6 centered near $\alpha = 0$ is a linear bar structure.

The presence of a bulge in the fiducial model prevents a significant bar from forming. The peak of the power at $\alpha_{max} = 12$ is significantly higher than the power at $\alpha = 0$. An identical simulation to the fiducial model was performed, with the only change being the removal of the bulge component of the galaxy. The Fourier decomposition for this bulgeless model at $t = 655$ Myr is also plotted on Figure 6. The amplitude of the trailing arms is slightly reduced and α_{max} is at smaller α , but the bar component of the disk has been greatly enhanced. The Fourier decomposition for the simulation with a spherical halo is also plotted for comparison. The spectrum of this model shows no significant peaks and is at low amplitude.

Fig. 5.— Smoothed particle image of the fiducial simulation at $t=655$ Myr. This and other images were created by smoothing the projected 2-d particle distribution with a Gaussian smoothing kernel before binning the particles in a 256×256 grid. In order to preserve fine structure while smoothing low-density regions, the width of the smoothing kernel is different for each particle, determined by the local particle density.

3.3. Growth of the Spiral Modes

Because the disk consists solely of collisionless particles, it is expected that the spiral modes excited by the halo should damp away simply due to relaxation effects. A galactic disk made entirely of stars could not sustain spiral patterns indefinitely, although since the potential of such a system is much smoother than our simulations the relaxation time would be much longer. We quantify “arm strength” as the sum of the amplitudes from $0 \leq \alpha \leq 25$. A strong bar would systematically bias this definition of arm strength, since $\alpha = 0$ represents linear structures. However, the simulations for which this calculation was done did not contain strong bars. The amplitude of the Fourier spectrum at $\alpha = 0$ in Figure 6 is not the dominant peak. Above $\alpha = 25$, which corresponds to a pitch angle of 4.6° , the Fourier spectrum is usually noise. Figure 7 plots arm strength against time for the fiducial simulation. It shows a rapid growth of the spiral modes, peaking around 0.5 Gyr, then exponentially decaying to an asymptotic value of around 0.5. The rms value of the arm strength for the model with the spherical halo is 0.2.

It is important to note that these simulations all begin with the disk being out of equilibrium with the triaxial halo. Several simulations were performed to test the response of the disk to

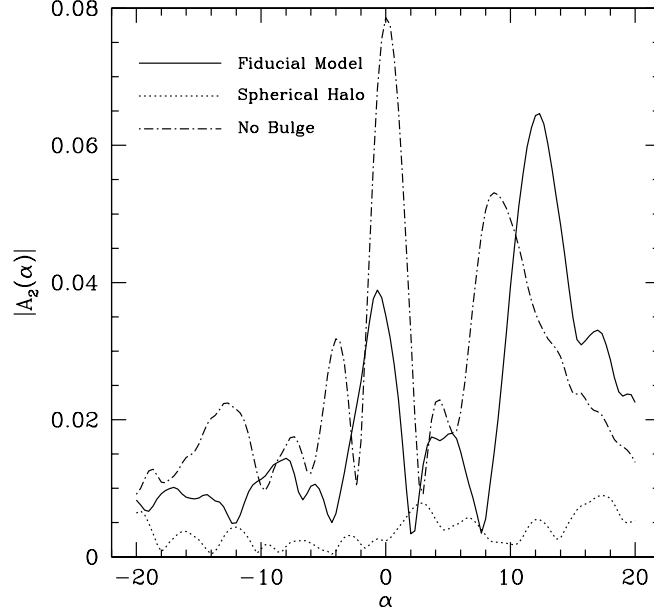


Fig. 6.— Fourier decomposition into logarithmic spirals for several variants of the fiducial model are plotted. The solid line shows the Fourier spectrum for fiducial model. The dash-dotted line shows the spectrum for the fiducial model without a bulge, which shows an enhanced bar component at $\alpha = 0$. The Fourier decomposition of the spherical-halo model is plotted with the dotted line, which returns just noise. All spectra shown are for $t = 655$ Myr.

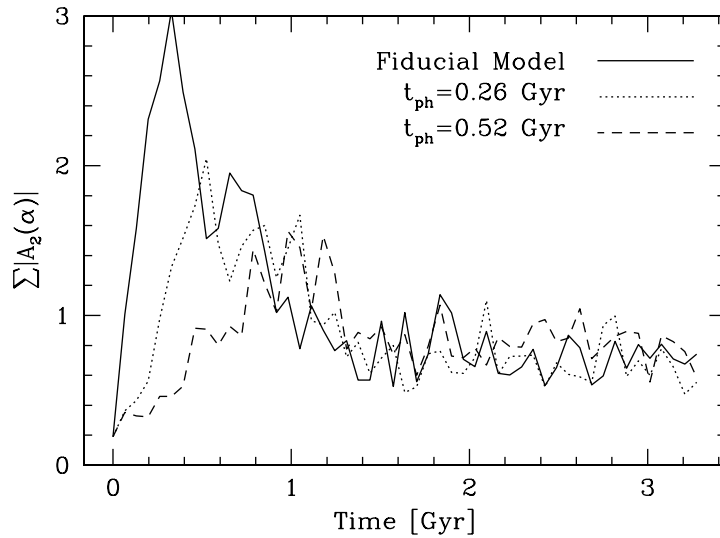


Fig. 7.— The strength of the spiral response of the fiducial model is plotted against time (*solid line*). The *dotted* and *dashed* lines represent models where the potential of the triaxial halo is phased in gradually over time. Phase times t_{ph} are given in the plot.

Fig. 8.— Same as Figure 5. The fiducial model, realized with 10^6 particles, is shown at $t = 655$ Myr. The scale of the image has been enlarged, with each axis being 15 disk scale lengths, rather than 10 in Figure 5. The inner Lindblad resonance, at $5h$, is plotted over the image.

a adiabatic conversion of the halo potential from spherical symmetry to the full triaxial form. Initially, the model is begun with the halo potential being spherical. The triaxial potential is phased in by the function

$$a_i = -(1 - \xi) \frac{GM_h}{(r_i + r_0)^2} - \xi \sum_{n,l,m} A_{nlm} \nabla \Phi_{nlm} \quad (13)$$

$$\xi = \left(\frac{t}{t_{ph}} \right)^2 \left(3 - 2 \frac{t}{t_{ph}} \right) \quad (14)$$

while $t < t_{ph}$. This function has zero derivatives at $t = 0$ and $t = t_{ph}$, so that the change in potential is smooth at the limits. Simulations were run with $t_{ph} = 20$ and 40 in N -body units, corresponding to physical times of 0.26 and 0.52 Gyr. These simulations, plotted in Figure 7, reach their peak arm strength near $2t_{ph}$ and then proceed to decay along the same curve as the fiducial model. The peak power is reduced monotonically with t_{ph} , from 2.5 to 1.7 and 1.2. All the curves in Figure 7 begin to overlap at a time of 0.8 Gyr and decay to the same arm strength thereafter. The structure is very similar in all three simulations at $t \geq 0.8$ Gyr. Even though the peak arm strength is reduced as the triaxial potential is phased in, the final state of the disk is unchanged.

3.4. Increasing the Simulation Resolution

To explore the N -dependence of our simulations, we increased the resolution of our fiducial model by an order of magnitude, realizing the disk with 10^6 particles and lowering the smoothing length to $\epsilon = 0.027$. In comparison to the $N = 10^5$ simulation, the structures in the disk, shown in Figure 8, are extremely apparent and well-resolved. Inside three scale lengths, strong $m = 2$ spiral arms are seen. These arms are encircled by two different structures at different radii. These are caustic-like structures, where the particle orbits from different radii have crossed each other, leading to a local density enhancement. The outer caustic is highly elliptical and is not continuous with azimuth. It has an axis ratio of 0.7 and a semimajor axis of $6.8h$. The inner caustic, which nearly connects with the spiral pattern inside it, has an axis ratio of 0.9 and a semimajor axis of $3.9h$. The inner Lindblad resonance for this model is shown on top of the image in Figure 8. Located just outside the inner caustic, at $5h$, it connects the inner and outer caustics at the minor axis of the outer caustic.

Figure 9 shows the Fourier decomposition of the $N = 10^6$ simulation in comparison to the fiducial model. The peaks in the power of both simulations are at the same locations, with a slightly higher peak at $\alpha = 12$ and lower peak at $\alpha = 0$ for the higher resolution simulation. Figure 9 also plots the arm strength as a function of time. The peak arm strength of the high resolution simulations is slightly higher than that of the fiducial simulation, and the two curves decay at nearly the same rate. These results demonstrate that the fiducial resolution is adequate

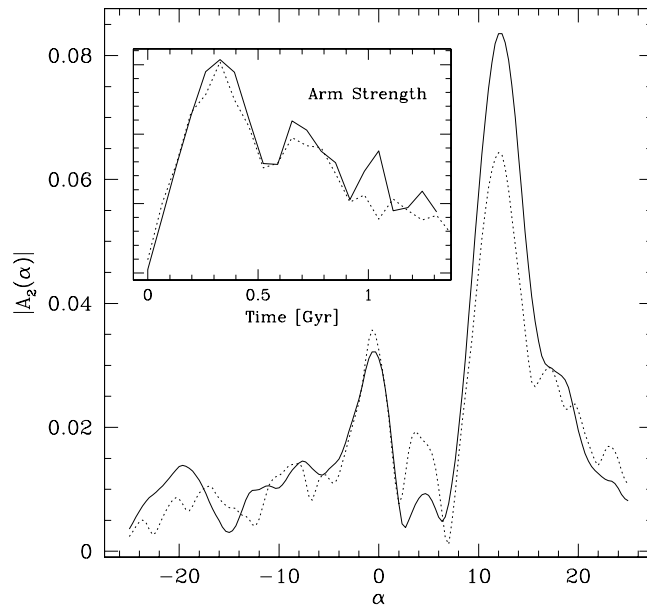


Fig. 9.— The Fourier decomposition of the fiducial model (*dotted line*), is compared to that of the simulation with $N = 10^6$ (*solid line*) at $t = 655$ Myr. The inset box compares the arm strength of both models.

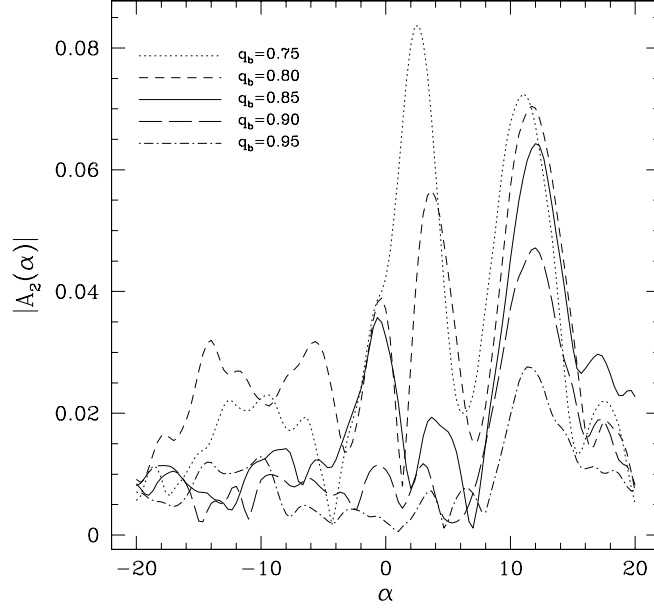


Fig. 10.— The Fourier decompositions for five simulations with different flattenings at $t = 655$ Myr. The peak in the spectrum at $\alpha = 12$ increases as the halo becomes more flattened. At $q_b < 0.85$, features at smaller α become comparable to the peak at $\alpha = 12$.

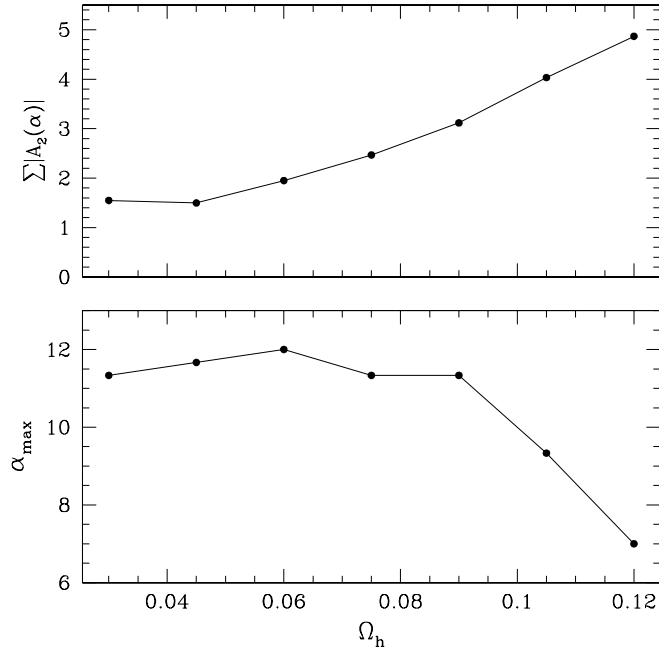


Fig. 11.— *Top Panel:* The arm strength of the disk, defined as the sum of the Fourier coefficients between $0 \leq \alpha \leq 25$, is plotted against the halo rotation rate, Ω_h . *Bottom Panel:* The location of the peak of the Fourier spectrum, α_{max} , is plotted against Ω_h . As the response of the disk increases, the peak in the spectrum moves to lower α , logarithmic spirals with higher pitch angle. All calculations were done at $t = 655$ Myr.

for the analysis performed.

3.5. Altering Halo Parameters

Cold dark matter simulations do not predict a single shape to dark matter halos; rather a distribution of axis ratios and triaxialities. For the halo figure rotation, the fiducial value of $\Omega_h = 0.06$ is somewhat arbitrarily chosen and limits on this parameter are not defined. We ran simulations to test the effects of varying these parameters, first varying q_b with Ω_h held constant, then varying Ω_h with q_b held at 0.85.

Figure 10 shows the Fourier decompositions of five models, including the fiducial model, with different levels of flattening. The most extreme model has $q_c = 0.5$ and $q_b = 0.75$. The most moderate model has axis ratios of 0.9 and 0.95. (The value of q_c for our models is always $2q_b - 1$.) All the models show a peak near $\alpha = 12$, showing that the pitch angle of the spiral arms created remains nearly the same in these different models. As q_b gets closer to unity, the response of the disk falls off; at $q_b = 0.95$, the amplitude of the Fourier peak is a factor of 2.3 lower than the fiducial model, and the disk itself shows little visible evidence for spiral structure. As q_b gets smaller, however, response of the disk around $\alpha = 0$ increases dramatically. In the most flattened model, the amplitude at $\alpha \sim 3$ is greater than that at $\alpha = 12$.

Figure 11 shows how the integrated arm strength and the value of α_{max} each change with the rotation rate of the halo, Ω_h . As the halo rotation increases, the response of the disk is monotonically increasing when $\Omega_h \geq 0.045$. As Ω_h increases to $\Omega_h = 0.12$, the value of α_{max} decreases from 12 to 7. This can be seen in Figure 12, which shows images of four of these models.

4. Exploring Parameter Space

The mass distribution of the Milky Way, although studied for several decades, is not known with certainty. The mass distribution of other galaxies are not known with much confidence at all, although it is known that there exists a range of halo and disk masses. Low surface brightness galaxies are thought to be dark-matter dominated, while many researchers espouse the maximal disk hypothesis presented by van Albada & Sancisi (1986) for galaxies with high surface brightness.

To explore these parameters, we constructed several sets of models in which all three components of a disk galaxy—disk, bulge, and halo—were varied in systematic ways. First we

Fig. 12.— Images are shown for four values of Ω_h : 0.045, 0.075, 0.09, and 0.12. The increased response of the disk, as well as the tighter spiral pattern, can be seen as the halo rotation rate is increased. The images represent the simulations at a time of 655 Myr.

explored models where the disk mass was reduced and the dynamics became more heavily influenced by the potential field of the halo. Second, we ran models where the parameters of the halo, namely the interior slope γ and the scale radius r_0 , were altered such that the mass distribution of the galaxy became disk-dominated at small radii. The total mass of the halo is constant, or nearly so, if one considers the truncation radius of the halo to be at a value of $100h$, the value chosen to calculate the moment of inertia of the halo. We characterize each of these models by its *mass ratio*, $(M_d/M_h)_{R_\odot}$, the ratio of the disk to halo mass within the solar radius, 8.5 kpc. Table 2 lists the general properties of the disk-dominated models, denoted D1–D5, where D5 is the most nearly maximal disk with a mass ratio of 4.53, and the properties of the halo-dominated models, denoted H1–H5, where H1 has the least massive disk with a mass ratio of 0.22. Figures 13 and 14 show the circular velocity profiles for the halo- and disk-dominated models respectively. In all models the bulge mass is set to $0.3M_d$.

Third, we created a set of models in which the disk and halo mass distributions were held constant and the bulge mass and scale length were varied. The disk mass was $M_d = 0.8$ and the halo parameters were the same as the fiducial model. The bulge masses were $M_b = 0, 0.1, 0.3, 0.5, 0.7, 0.9, 1.3$, and 2.0 . The value of each r_b was calculated such that the average density inside one bulge scale radius was the same as that of the fiducial bulge, namely

$$r_b = r_{b,0} \left(\frac{M_b}{M_{b,0}} \right)^{1/3} \quad (15)$$

where $r_{b,0}=0.2$ and $M_{b,0} = 0.3$.

Our last set of models centered on models that had lower rotation velocities, values closer to 100 km s^{-1} than to the fiducial value of 220 km s^{-1} . The motivation behind these models will be discussed in §6. The specific parameters used are as follows: The halo parameters are identical to the halo in model D5, which is the model with the lowest central concentration. The disk mass was 0.5. The bulge mass was varied, having values of 0, 0.075 and 0.15.

The results of these simulations will be discussed in the following two sections, focusing on the formation of bars and morphology of the spiral arms induced in the disk by the halo.

5. Bar Formation

Bars are simple to detect in our simulations, since they represent the $\alpha = 0$ modes of the Fourier decompositions. Models with strong spiral arms, however, can also return high amplitudes at $\alpha = 0$ compared to models with no structure at all. To prevent false detection of bars, we followed the procedure described in Efstathiou et al. (1982) to quantify the strength of the bar. The particles are binned in radial rings of linear separation and the amplitude and phase of the $\alpha = 0, m = 2$ component is calculated for each ring. If a bar is present, it is defined as existing

Table 1. Properties of the Fiducial Simulation

Disk Properties	Halo Properties	Bulge Properties
$M_d = 1.0$	$M_h = 6.0$	$M_b = 0.3$
$h = 1.0$	$R_0 = 3.63$	$r_b = 0.2$
$z_0 = 0.2$	$\gamma = 1.0$	$\gamma = 1.0$
	$q_b = 0.85$	
	$q_c = 0.70$	
	$\Omega_h = 0.06$	

Table 2. Properties of the Models with Different Mass Distributions

Halo-Dominated Models			Disk-Dominated Models			
Model Name	$(M_d/M_h)_{R_\odot}$	M_d	Model Name	$(M_d/M_h)_{R_\odot}$	γ	r_0
H1	0.22	0.3	D1	0.91	0.8	3.63
H2	0.38	0.5	D2	1.13	0.6	3.73
H3	0.53	0.7	D3	1.51	0.4	3.98
H4	0.68	0.9	D4	2.27	0.2	4.48
H5*	0.76	1.0	D5	4.53	0.0	5.69

Note. — (*) Model H5 is the fiducial model described in §3

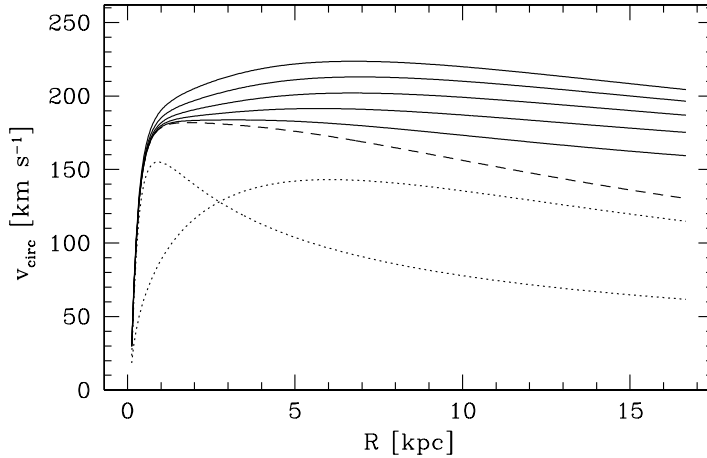


Fig. 13.— Circular velocity curves for models D1–D5 (disk-dominated) are plotted. The dotted lines represent the contributions to the circular velocity from the disk and the bulge. The dashed line is the combined circular velocity of the disk and bulge. The solid lines are the total circular velocities of the five models. The lowest curve, which is closest to a maximal-disk model, is D5. The highest curve is model D1. The specific halo parameters used to create these models are listed in Table 2.

within the rings that have phases which are coherent to within 10%. The bar strength is the maximum Fourier component within this coherence and is denoted by the symbol δ_2^{max} . The rings are $0.1h$ in width and contain several thousand particles each. To be considered a valid detection, the coherence must be at least 5 rings in length but does not have to begin at the center—most simulations with obvious bars do not begin having coherent phases until $R \sim 0.3 - 0.5h$. From this method we can determine the amplitude, length, and pattern speed of the bar. The binning of particles in cylindrical rings eliminates false detection of bars in simulations with strong spiral patterns because these models will have high values of δ_2^{max} but will not have coherent phases.

Figure 15 shows simulations at four different levels of bar strength: $\delta_2^{max} = 0.1, 0.2, 0.4$, and 0.6 . Values of δ_2^{max} less than or equal to 0.2 have weak bars that are generally ~ 1 disk scale length in size. At $\delta_2^{max} = 0.4$, the bar is very distinct and longer. At $\delta_2^{max} = 0.6$, the highest value seen in our simulations, the bar dominates the mass of the disk and can be nearly four scale lengths in size. When integrated with spherical halos, all of the models presented in this section developed no detectable bars.

Figure 16 shows the time evolution of bar strength in models with different values of halo rotation rate. For the fiducial value of $\Omega_h = 0.06$, the disk-dominated models are generally stable. Only model D3 develops a detectable bar, one which asymptotes to $\delta_2^{max} \sim 0.15$. When Ω_h is increased, however, bar instabilities become much larger. At $\Omega_h = 0.075$, the models with the lowest mass ratios (D1 and D2) are stable, but the other models show significant bar formation.

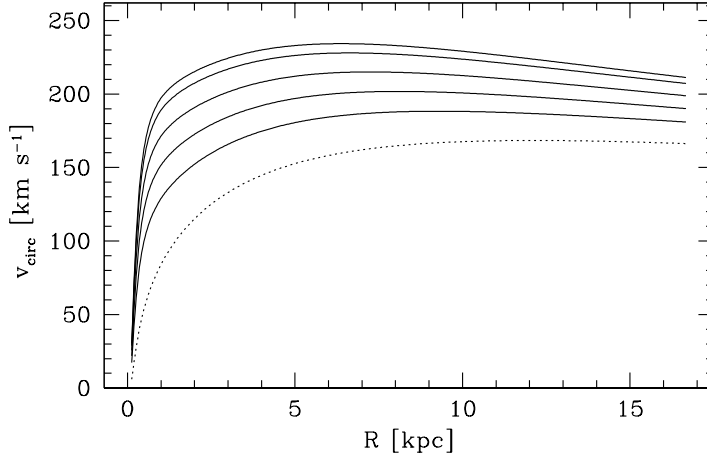


Fig. 14.— Circular velocity curves for models H1–H5 (halo-dominated) are plotted. The dotted line represents the circular velocity of the halo, which is constant in all these models. The solid lines are the total circular velocity from the disk, halo and bulge. Model H1, with a disk mass of 0.3, is the lowest curve; Model H5, which is the fiducial model, is the highest. For each model, the bulge mass $M_b = 0.3M_d$.

The growth in the bar modes is very gradual at first, but at 3 Gyr models D3, D4, and D5 rapidly grow their bars, which peak at values of δ_2^{max} between 0.5 and 0.6 and slowly decline in amplitude. In the bottom panel of Figure 16, Ω_h has been increased to 0.09. All the models begin to show bar structures at ~ 2.5 Gyr and become bar-dominated by 3 Gyr. Models D3 and D4 make a rapid transformation to being bar-dominated, while δ_2^{max} for the other models grow more gradually. Regardless of the time it takes for the bar to grow, the values of δ_2^{max} for all the models is close to 0.4 once the bar has reached its peak strength. The values of $\langle \delta_2^{max} \rangle$, the bar strength averaged over the last 0.8 Gyr of the simulation, do not show any correlation with mass ratio. For model D1, $\langle \delta_2^{max} \rangle = 0.39$, while for model D5 $\langle \delta_2^{max} \rangle = 0.40$. The halo-dominated models, including the fiducial model H5, are all stable against bar formation, even with a halo rotation rate of 0.09.

As stated above, the stability of the disks shown in Figure 16 is in part due to the mass of the bulge. We decreased the value of the bulge mass to $0.15M_d$ and re-ran our disk-dominated models to investigate bar formation in galaxies with less prominent bulges. Figure 17 shows the results. At $\Omega_h = 0.06$, models D3–D5 develop distinct bars while the other models remain stable. At $\Omega_h = 0.075$, all the models show some level of bar strength, with the average value of δ_2^{max}

Fig. 15.— Images of four simulations at increasing levels of bar strength, δ_2^{max} . The values of δ_2^{max} are printed above each panel. In contrast to the fiducial resolution, all simulations used in this figure has a resolution of 3×10^5 . The higher resolution was used to reduce noise which can be amplified in longer simulations. The statistics calculated in Figures 16 and 17 used higher resolution simulations.

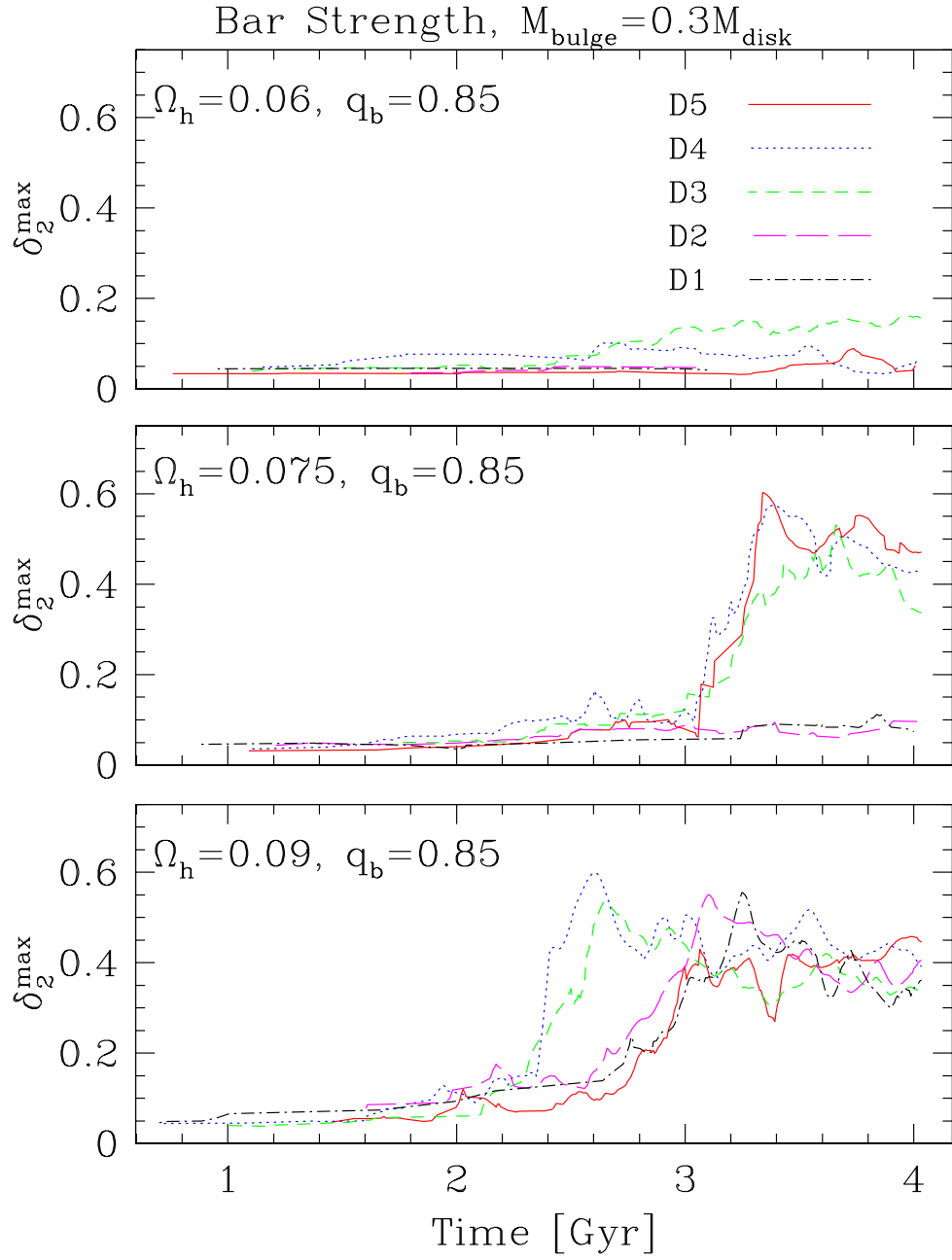


Fig. 16.— The bar strength for models D1–D5 are plotted as a function of time at three different values of Ω_h .

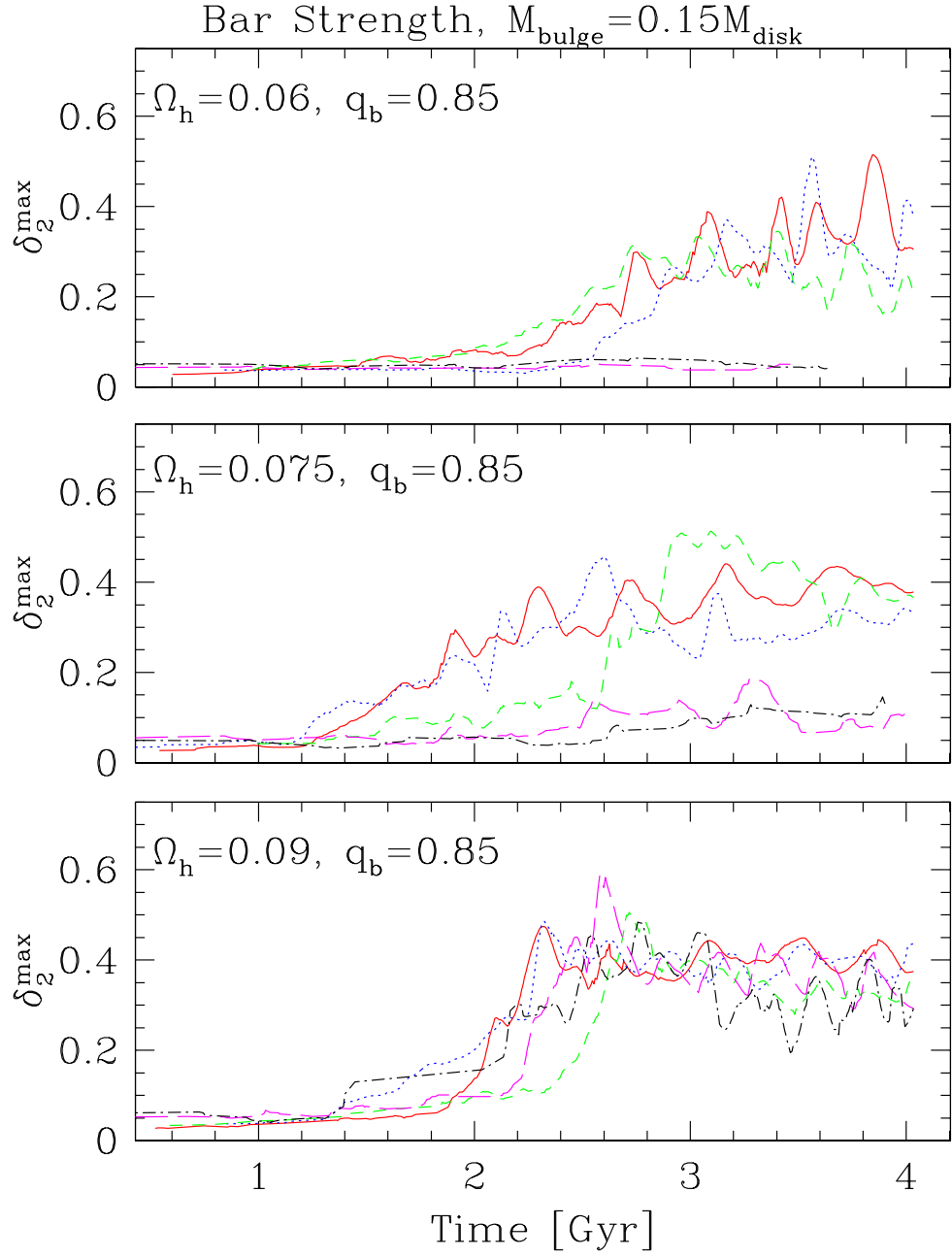


Fig. 17.— Same as Figure 16. The bulge mass for these models has been reduced to 0.15 to make the models less stable against bar formation. The different line styles represent the same models as in Figure 16.

loosely correlating with increasing mass ratio. At $\Omega_h = 0.09$, all the models show rapid bar growth and become bar-dominated between 2 and 2.5 Gyr. The values of $\langle \delta_2^{max} \rangle$ also correlate roughly with mass ratio. For model D1 $\langle \delta_2^{max} \rangle = 0.30$, increasing to $\langle \delta_2^{max} \rangle = 0.41$ for model D5. In these simulations, the growth of the bar begins earlier but is slower than the models with $M_b = 0.3M_d$. The values of $\langle \delta_2^{max} \rangle$ are slightly higher in the $M_b = 0.3M_d$ simulations for those models which develop bars.

The bar pattern speeds do not appear to correlate with either Ω_h or δ_2^{max} . The simulations that develop strong bars all have bar pattern speeds near 0.5 radians per unit time (in the same units as Ω_h). The pattern speeds do not change on average once the bar has reached its peak amplitude. Since our simulations employ a static halo potential our results do not reflect the dynamical friction and angular momentum transfer that would surely occur in physical galaxies, reducing the pattern speed (Debattista & Sellwood 2000; Valenzuela & Klypin 2002).

6. Spiral Morphology

6.1. Spiral Arm Pitch Angle

Although in some simulations the peak in the Fourier spectrum is well defined and narrow, in others a simple search for the maximum value of $|A_2|$ can vary significantly in time if there is more than one peak in the spectrum. Pitch angles in spiral galaxies are known to vary with radius and are measured as an average value (Kennicutt 1981). Therefore, to quantify the morphology of the spiral structure in our simulations we calculate an average value of α , summed from $0 \leq \alpha \leq 25$ and weighted by the Fourier amplitude at each value of α . The simulations for which this quantity, $\langle \alpha \rangle$, were calculated did not contain bars as defined in §5, and so using $\alpha = 0$ as the starting point of the weighted average does not bias the results to smaller values of $\langle \alpha \rangle$. Only amplitudes greater than half the rms amplitude in that range are actually counted in the summation. The value of $\langle \alpha \rangle$ varies in time about a mean value at a level of ~ 5 -20%. Fourier spectra with higher overall amplitude, usually found in models with higher values of Ω_h , have smaller rms fluctuations. The weighted average of α is again averaged over the time range 0.4–1.3 Gyr. The lower of these limits is chosen to allow the disk to reach equilibrium with the halo. As the simulations progress the arm strength decays, and so the integrations were stopped at 1.3 Gyr. In our notation, $\langle \alpha \rangle$ is the weighted average of the Fourier spectrum for a given moment in time, and $\langle \alpha \rangle_t$ is the average of this value over time range mentioned. The quantity $\langle \alpha \rangle_t$ can then be converted into an average pitch angle, $\langle p \rangle$.

The top panel in Figure 18 shows the evolution of $\langle p \rangle$ with time for the halo-dominated models H1–H5 with $\Omega_h = 0.09$. Although there is some variation, the average value with time for each simulation is well-defined. The bottom panel in Figure 18 shows four realizations of the low-velocity model with $M_b = 0.3M_d$, the last of which was resolved at 3×10^5 particles rather than the fiducial value of 10^5 . The simulations were sampled with much higher frequency to

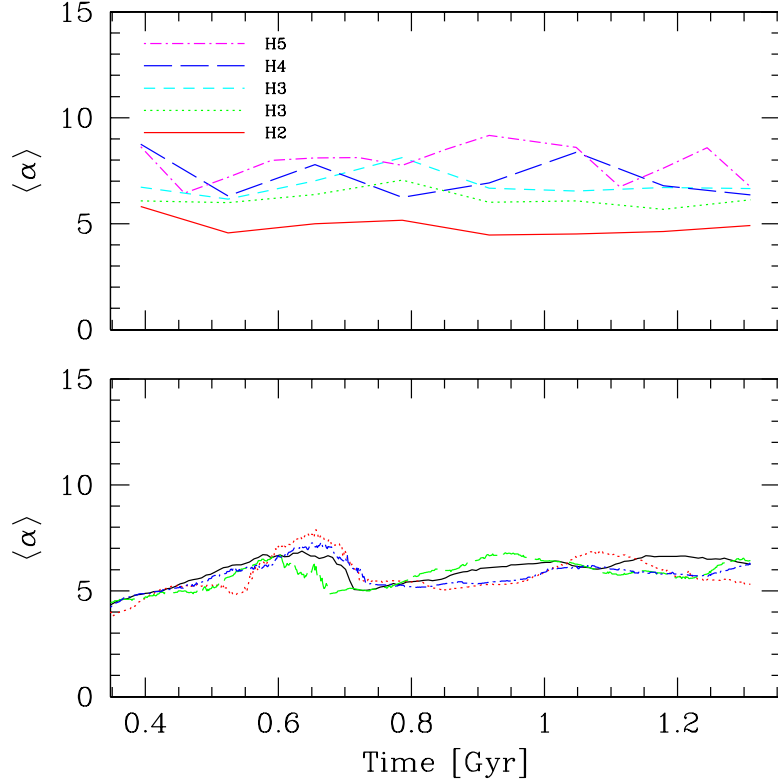


Fig. 18.— *Top Panel:* The weighted average of the Fourier spectrum, $\langle \alpha \rangle$, is plotted against time for models H1–H5 and a halo rotation rate of 0.09. The values of $\langle \alpha \rangle$ for each model remain nearly constant in time for 1 Gyr. *Bottom Panel:* $\langle \alpha \rangle$ is plotted against time for four realizations of the low-velocity model described in §4 with $M_b = 0.3M_d$. The black line represents a simulation resolved with $N = 3 \times 10^5$. The other lines represent simulations with the fiducial resolution of 10^5 . The time range shown is the range used when calculating the time average, $\langle \alpha \rangle_t$, which is then used to calculate the average pitch angle, $\langle p \rangle$.

investigate how $\langle \alpha \rangle$ varies on small time scales. The results show little difference between all four realizations, showing that one realization at the fiducial resolution, although not ideal, is adequate for our results.

The clear trend in the top panel of Figure 18 is that $\langle \alpha \rangle$ decreases with decreasing mass ratio. Figure 19 shows the value of $\langle \alpha \rangle_t$ plotted against mass ratio for all the models listed in Table 2. The results for $\Omega_h = 0.09$ have smaller error bars than those for $\Omega_h = 0.06$ because of the higher amplitude of the Fourier spectra for $\Omega_h = 0.09$. For both sets of simulations, the value of $\langle \alpha \rangle_t$ is maximum at the fiducial mass ratio of 0.76 and decreases as the mass ratio gets bigger or smaller. As expected from the results of Figure 11, the data for $\Omega_h = 0.09$ are shifted to lower values of $\langle \alpha \rangle_t$ as compared to the data for $\Omega_h = 0.06$. Figure 20 shows images of models H1–H4 at 655 Myr with $\Omega_h = 0.09$. The increased response of the disk with decreasing mass ratio is clearly evident.

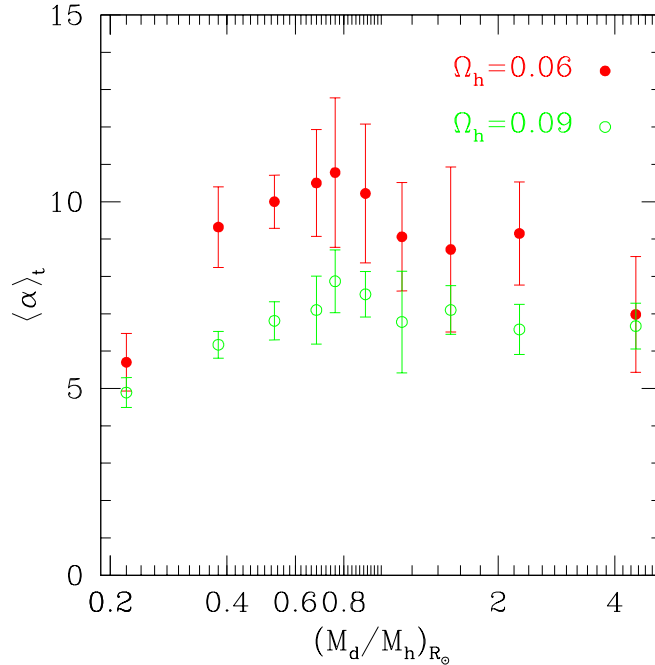


Fig. 19.— The time average of the Fourier spectrum, $\langle \alpha \rangle_t$, is plotted against mass ratio for all models listed in Table 2. The different plot symbols represent different halo rotation rates, 0.06 and 0.09. The error bars are standard deviations of the values of $\langle \alpha \rangle$ averaged to calculate $\langle \alpha \rangle_t$. The error bars for the simulations with $\Omega_h = 0.06$ are larger because of the lower overall amplitude of the Fourier spectra at lower Ω_h , allowing more noise into the calculations.

The spiral structure for model H2 can be traced for well over 2π radians. The image of model H1, with the lowest mass disk, resembles a classic Kalnajs disk (e.g. Binney & Tremaine 1987). The caustic structures seen in the high-resolution run of the fiducial simulation are seen throughout the disk and are highly elliptical. Differential rotation has caused the oval caustics to overlap and create a spiral pattern.

6.2. Bulge to Disk Ratio and the Hubble Sequence

The third set of models described in §4, those with varying bulge mass, can be thought of as an ersatz Hubble sequence, at least along one dimension of the required criteria. The properties of the disk and halo were chosen as to produce significant amplitudes in the Fourier decomposition, reducing noise in the measured value of the pitch angle.

Fig. 20.— Images of models H1–H4 at a time of 655 Myr. These simulations all have $\Omega_h = 0.09$. The mass of each disk is printed above each panel. The mass of the bulge is $M_b = 0.3M_d$ for each model.

Figure 21 shows images of four models, $M_b = 0.1, 0.3, 0.9$ and 2.0 with $\Omega_h = 0.105$. As the bulge mass varies from small to large, the spiral arms vary from loosely to tightly wound. The arms themselves vary in thickness; the larger the bulge mass, the narrower the spiral arms. For the model with $M_b = 0.1$, the spiral arms can be traced to within one scale radius of the center. For $M_b = 2.0$, the arms do not begin until outside two scale radii (although a high-resolution simulation could reveal structure inside this radius, as it did for the fiducial simulation). Figure 22 plots the average pitch angle $\langle p \rangle$ against the logarithm of the bulge-to-disk ratio for each of these models. (Except for the model with $M_b = 0$ of course, which had pitch angles of 16.6° and 23.1° for the halo rotation rates 0.075 and 0.105 respectively.) The plot shows a linear increase in $\langle p \rangle$ with $\log(M_b/M_d)$. As the bulge mass increases, the spiral arms become tighter. The pitch angles for the simulations with $\Omega_h=0.105$ are systematically higher than those with $\Omega_h=0.075$. Plotted as well are data taken from Kennicutt (1981) for the pitch angles of galaxies along the Hubble sequence, from Sa-type to Sc-type. The bulge-to-disk ratios corresponding to these classifications were taken from Köppen & Arimoto (1990). The scatter in the observations, mentioned at the top of this section, is easily apparent.

The simulation data, however, follow the average trend of pitch angle with Hubble type. The slopes of the simulation data are flatter than that of the observations. Several explanations are viable for explaining this: The simulated Hubble sequence created here is artificial since it only varies one parameter, the bulge mass. There could be systematic variations of total galaxy mass and length scales along the Hubble sequence which could effect the spiral response of the disk. Only two values of Ω_h were used, and the steeper slope of the observations could be reproduced if it were assumed that higher bulge mass correlated with lower halo rotation rates. Lastly, our definition of $\langle \alpha \rangle$, since it is an average over a range of α , would tend to return values that are closer to the center of that range, reducing the slope of the correlation. The pitch angles in Kennicutt (1981) were measured by obtaining the arm coordinates from H α or blue continuum observations and plotting these coordinates on the $\log r$ vs ϕ plane. A straight line was fitted to each arm and the results for the two main arms were averaged.

6.3. Pitch Angle and Rotational Velocity

As noted above, a better predictor than Hubble classification of spiral pitch angle is the rotational velocity of the galaxy (Kennicutt 1981). The relation found in the Kennicutt paper is plotted by the solid lines in Figure 23. These lines represent the mean and upper and lower bounds on his data. The slope and intercept of these lines were calculated by inspection, and are not meant to be quantitatively compared to our simulation results. Qualitatively, however, it

Fig. 21.— Images of models with bulge masses $M_b = 0.1, 0.3, 0.7$, and 2.0 . For all simulations, $M_d = 0.8$ and $\Omega_h = 0.105$.

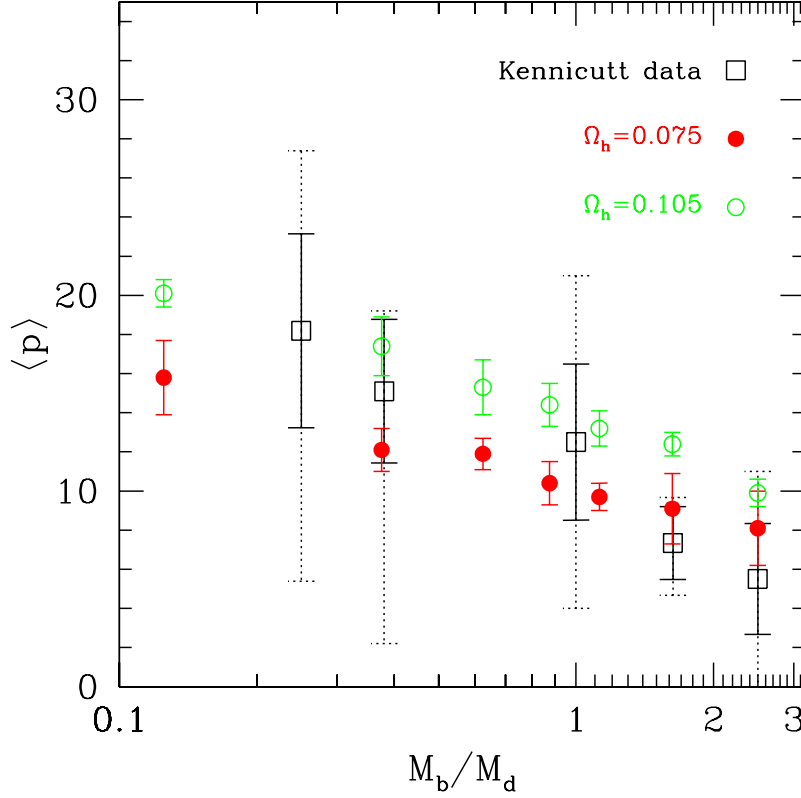


Fig. 22.— The average pitch angle, $\langle p \rangle$, is plotted against bulge-to-disk ratio for the models described in §6.2. The different solid plot symbols represent different halo rotation rates, 0.075 and 0.105. Error bars are statistical. The open squares represent data taken from Kennicutt (1981) of pitch angles for Hubble types Sa, Sab, Sb, Sbc, and Sc. The solid error bars are the standard deviations of these data. The dotted error bars are the high and low values of pitch angle for each Hubble type.

is obvious that our simulations follow the same relation. Both sets of bulge simulations lie well within the bounds set by the observations. What is remarkable as well is that the simulations listed in Table 2 also show this trend. The simulations with the lower rotation velocity generally have higher pitch angles. Although the halo-dominated models do not return the same pitch angles as the disk-dominated models with the same rotation velocity, the trend is still preserved regardless of whether the mass dominating the kinematics is from the halo or the disk or the bulge. The scatter in our results lies within the scatter seen observationally.

The lowest rotation velocity in the models listed in Table 2 is D5, with $v_{rot} = 165 \text{ km s}^{-1}$. To explore the response of systems with even lower velocities, we used the models described at the end of §3 with both low mass disks and halos. Three different bulge masses were used: $M_b = 0$, $0.15M_d$ and $0.3M_d$. The first two of these models developed a strong and a weak bar respectively. The method of bar detection used in §4 allowed us to eliminate the particles that contribute to

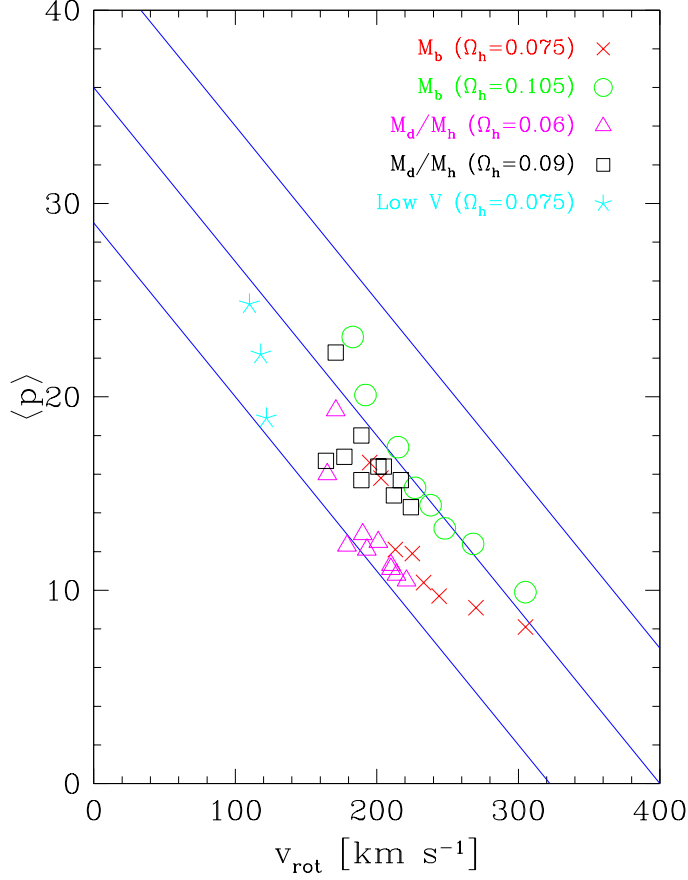


Fig. 23.— The average pitch angle, $\langle p \rangle$, is plotted against the maximum rotational velocity, v_{rot} , for each simulation. Five sets of models are plotted: M_b means a set where the bulge mass is the varying quantity. M_d/M_h means a set where the mass ratio is varying. *Low V* means models designed to have low rotational velocity. Descriptions of all these models can be found in §4. The solid lines were taken from visual inspection of data in Kennicutt (1981), representing the mean and the upper and lower bounds of the majority of the observational data (excluding obvious outliers).

the bar from being used in calculating $\langle \alpha \rangle$. Since the length of the bar is known, all particles with radii below the bar length were simply not counted in the summation in equation (12). The results are plotted in Figure 23, and they follow the observational relation.

A tighter correlation can be achieved by including what we know of the mass distribution and halo rotation. Figure 24 plots $\langle p \rangle$ against the “normalized” torque of the halo, a dimensionless quantity given by

$$\tau' = \tau_{R_*}^{1/2} / (v_{\text{rot}} M_{R_*}^{1/2}), \quad (16)$$

where τ is torque, v_{rot} is the maximum rotation velocity of the disk also used in Figure 23, and M

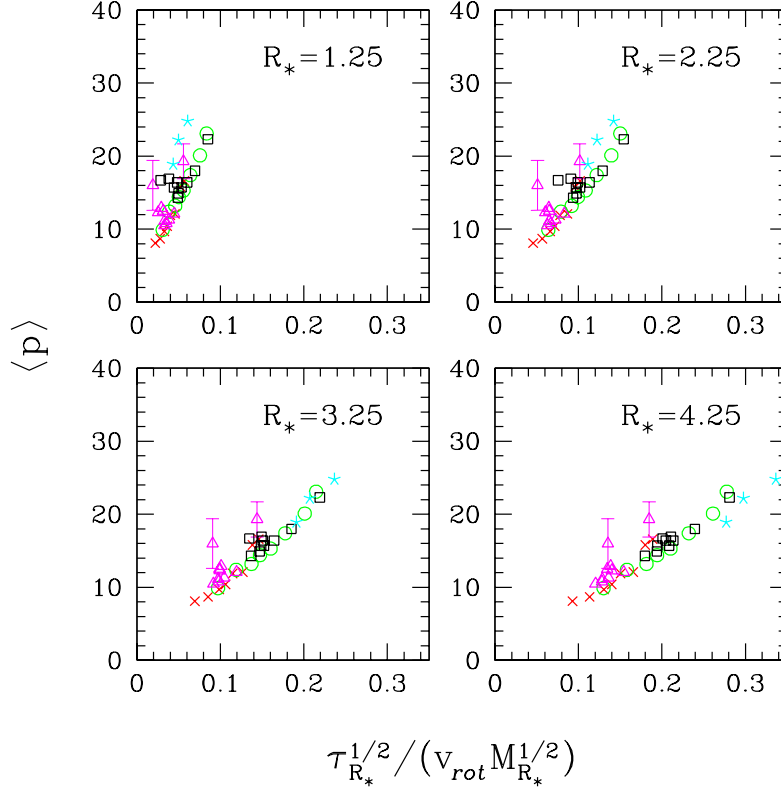


Fig. 24.— The average pitch angle is plotted against the normalized torque for the same models shown in Figure 23. The plot symbols are the same as Figure 23. The radius R_* at which τ' is calculated is shown in the top right of each panel. For $R_* = 3.25$, all the model sets form the tightest correlation, with the main outliers being from the set with varying mass ratio with $\Omega_h = 0.06$, which has the largest error bars of all the sets. The points with error bars are the same models in each panel. The error bars for the two outliers are larger than the typical error by a factor of 2-3. The errors for $\langle p \rangle$ were calculated by differential error on the relation between pitch angle and α , using the statistical error of $\langle \alpha \rangle_t$.

is the total mass of the galaxy. The torque in the right hand side of equation (16) is the torque of the halo, $\tau = I\Omega_h^2$, where I is the moment of inertia of the halo. The subscript R_* on the torque and the total mass represents the radius at which these two quantities are calculated. The four windows in Figure 24 plot $\langle p \rangle$ against τ' calculated at four different values of R_* . The correlation is apparent in all four panels, but is excellent for $R_* = 3.25$.

The choice of R_* significantly influences the slope of the correlation, with smaller values of R_* resulting in steeper slopes. The scatter changes only moderately with varying R_* for the first four sets of models in Figure 24, but effects the low-velocity models most. The quantity τ' has a power-law dependence on R_* , which is highest with the low-velocity models. Thus the values of τ' for that set will be affected most by changes in R_* .

7. Discussion

We have presented simulations of galaxy disks embedded in rigid, rotating, triaxial halos. We have constructed a suite of models in which the masses of the disk, bulge and halo have all been varied. With these models, the effects of changing the halo rotation rate and flattening have been investigated. Our results have focused on the formation of bars and spiral structure. Models with a mass ratio $(M_d/M_h)_{R_\odot} > 0.8$ and $\Omega_h = 0.09$ develop a strong bar, even if a significant bulge is present. For all models, the torque created by the halo induces spiral structure in the disk. The average pitch angle of this structure, $\langle p \rangle$, is strongly anti-correlated with the maximum rotation speed of the model.

It is clear that estimations of the stability of disk galaxies cannot ignore the shape of the halo. Models with significant amounts of dark matter and a significant bulge (like D1 and D2, which have rotational velocities of over 200 km s^{-1} in our system of units) can become bar dominated with halo rotation rates of $\Omega_h = 0.09$ and greater. Maximal disk models, like D5, are very susceptible to bar instabilities if torqued by the halo. In all the simulations presented in §5, the only set of halo and bulge parameters for which models D3–D5 were stable against bar formation was $M_b = 0.3M_d$ and $\Omega_h = 0.06$. Even with those parameters, model D3 still developed a low amplitude but persistent bar. A simple criterion for determining whether a disk galaxy will develop a bar, such as that determined by Efstathiou et al. (1982), is not readily apparent from the data. With more free parameters, M_b , q_b , and Ω_h , in our simulations, it may be that a simple criterion cannot quantify the stability of all our models used in our simulations.

The correlation of rotational velocity and pitch angle in our models provides a physical explanation of the same correlation found in observations of spiral galaxies. The pitch angle of the arms induced by an external torque is related to the total mass of the system, loosely through v_{max} , but more tightly to the dimensionless torque parameter τ' . The differences seen in our results for different halo rotation rates and flattenings fit well with the amount of scatter seen in the correlation of v_{max} with $\langle p \rangle$ for real galaxies. This result does not have to be unique to the properties of a galaxy’s halo; it has been shown that encounters with satellite galaxies, which would also create a time-varying potential field in which to disrupt the disk, induce two-armed spiral structure in disk galaxies (e.g. Toomre & Toomre 1972). But encounters with smaller galaxies are by their nature transient and it remains that spiral structure is a ubiquitous feature of disk galaxies both with and without satellite perturbers.

In Kennicutt (1981), and references therein, the properties of the spiral arms are measured through their blue light, usually from HII regions, dust lanes, or the blue continuum, all of which are associated with star formation. Our collisionless simulations better represent the red stellar population which accounts for most of the mass in a galactic disk. Images of spiral galaxies in the near infrared have shown that spiral structure is evident in old stellar populations (Eskridge et al. 2002). The arms observed are smoother and wider than those seen in blue light, but generally follow the same morphology.

The Fourier decomposition method used in this paper has been applied to observational data of HII regions in spiral galaxies (Puerari & Dottori 1992; García-Gómez & Athanassoula 1993). The Fourier spectra obtained resemble in many ways the spectra of our simulated galaxies, often with several distinct peaks inside one spectrum. The pitch angle was calculated by these authors from the value of α for which the amplitude is highest. This definition of p reproduces the general trend with Hubble type as described by Kennicutt (1981) but does not reflect the natural variations in pitch angle within a single galaxy seen both in the Fourier spectra of the observations and in Kennicutt’s calculations. Kennicutt noted that the variations of p for a typical galaxy were significantly larger than the measurement error. An average value of the pitch angle better represents the multiple spiral components.

Hydrodynamic simulations by Bekki & Freeman (2002) have shown that the extended spiral structure seen in the blue compact dwarf galaxy NGC 2915 could be due to a rotating triaxial halo. Their simulations contained a disk fully composed of gas particles and a halo 100 times more massive than the disk, effectively making the disk massless. Our collisionless simulations show spiral structure in the inner regions of galactic disks. Since gas fractions in disk galaxies are usually no higher than 30%, the gas should be gravitationally coupled to the stars and follow the spiral patterns seen in our simulations. The dissipation and subsequent star formation in the gas would lead to self-consistent spiral structure which would outlast a collisionless disk and work to preserve its structure as well.

An open question is the correct value or range of values to use for Ω_h . The figure rotation of NGC 2915 has been calculated to be $8.0 \text{ km s}^{-1} \text{ kpc}^{-1}$ (Bureau et al. 1999), which is 0.107 in our N -body units. These authors also propose that halo figure rotation, a distinct phenomenon from halo angular momentum, is present in a significant fraction of dark matter halos in CDM simulations.

Regardless of the details in determining Ω_h or $\langle p \rangle$, it has been clearly demonstrated that an external torqueing mechanism can reproduce the type of correlation observed between spiral pitch angle and rotational velocity. Even in simulations in which the magnitude of the applied torque is the same, *i.e.* the density profile, flattening, and rotation rate of that halo are all held constant, the pitch angle of the spiral structure varies according to the total mass of the system.

JLT would like to thank Richard Pogge for his helpful discussions, as well as Volker Springel and Stein Sigurdsson for help with the GADGET and SCF codes respectively. This work was performed at the Ohio Supercomputer Center under grant PAS0825.

REFERENCES

- Alam, S.M.K. & Ryden, B.S. 2002, *ApJ*, 576, 610
 Barnes, J.E. & Hut, P. 1986, *Nature*, 324, 446

- Barnes, J.E. 1992, *ApJ*, 393, 484
- Binney, J. & Tremaine, S. 1987 *Galactic Dynamics* (Princeton Univ. Press)
- Bureau, M., Freeman, K.C., Pfizner, D.W., & Meurer, G.R. 1999, *AJ*, 118, 2158
- Dubinski, J. & Carlberg, R.G. 1991, *ApJ*, 378, 996
- Dubinski, J. 1994 *ApJ*, 431, 617
- Dubinski, J., Mihos, J.C., & Hernquist, L. 1999, *ApJ*, 526, 607
- Efstathiou, G., Lake, G., & Negroponte, J. 1982, *MNRAS*, 199, 1069
- Eskridge, P.B., et al. 2002, *ApJS*, accepted, (astro-ph/0206320)
- García-Gómez, C. & Athanassoula, E. 1993, *A&AS*, 100, 431
- Holh, F. 1976, *AJ*, 81, 30
- Hernquist, L. 1990, *ApJ*, 356, 359
- Hernquist, L. 1993, *ApJS*, 86, 389
- Hernquist, L. & Ostriker, J.P. 1992, *ApJ*, 386, 375
- Holley-Bockelmann, K., Mihos, J.C., Sigurdsson, S., & Hernquist, L. 2001, *ApJ*, 549, 862
- Huntley, J.M., Sanders, R.H., & Roberts, W.W. 1978, *ApJ*, 221, 521
- Ibata, R., Lewis, G.F., Irwin, M., Totten, E., & Quinn, T. 2001, *ApJ*, 551, 294
- Jing, Y.P. & Suto, Y. 2002, *ApJ*, 574, 538
- Kennicutt, R.C. 1981, *AJ*, 86, 1847
- Kennicutt, R.C. & Hodge, P. 1982, *ApJ*, 253, 101
- Köppen, J. & Arimoto, N. 1990, *A&A*, 240, 22
- Lin, C.C. 1970, in *IAU Symposium No. 38: The Spiral Structure of our Galaxy*, ed. Becker and Contopoulos (Dordrecht: Reidel), p 377
- Mihos, J.C. & Hernquist, L. 1996, *ApJ*, 464, 641
- Merritt, D. & Quinlan G.D. 1998, *ApJ*, 498, 625
- Murali, C., Katz, N., Hernquist, L., Weinberg, D.H., & Davé, R. 2002, *ApJ*, 571, 1
- Navarro, J.F., Frenk, C.S., & White, S.D.M. 1997, *ApJ*, 490, 493
- Ostriker, J.P. & Peebles, P.J.E. 1973, *ApJ*, 186, 467
- Puerari, I. & Dottori, H.A. 1992, *A&AS*, 93, 469
- Ryden, B.S. 1992, *ApJ*, 396, 445
- Ryden, B.S. 1996, *ApJ*, 461, 146
- Sanders, R.H. & Huntley, J.M. 1976, *ApJ*, 209, 53
- Sanders, R.H. 1977, *ApJ*, 277, 916

- Sanders, R.H. & Tubbs A.D. 1980, ApJ, 235, 803
- Sellwood, J.A. & Athanassoula, E. 1986, MNRAS, 221, 195
- Sellwood, J.A. & Sparke, L.S. 1988, 231, 25
- Siegel, M.H., Majewski, S.R., Reid, I.N., & Thompson, I.B. 2002, ApJ, accepted (astro-ph/0206323)
- Springel, V. 2000, MNRAS, 312, 859
- Springel, V., Yoshida, N., & White, S.D.M. 2001, NewA, 6, 79
- Thakar, A.R. & Ryden, B.S. 1998, ApJ, 506, 93
- Toomre, A. & Toomre, J. 1972, ApJ, 178, 623
- Tremblay, B. & Merritt, D. 1996, AJ, 111, 2243
- Warren, M.S., Quinn, P.J., Salmon, J.K., & Zurek, W.H. 1992, ApJ, 399, 405

This figure "figure5.jpg" is available in "jpg" format from:

<http://arxiv.org/ps/astro-ph/0209165v1>

This figure "figure8.jpg" is available in "jpg" format from:

<http://arxiv.org/ps/astro-ph/0209165v1>

This figure "figure12.jpg" is available in "jpg" format from:

<http://arxiv.org/ps/astro-ph/0209165v1>

This figure "figure15.jpg" is available in "jpg" format from:

<http://arxiv.org/ps/astro-ph/0209165v1>

This figure "figure20.jpg" is available in "jpg" format from:

<http://arxiv.org/ps/astro-ph/0209165v1>

This figure "figure21.jpg" is available in "jpg" format from:

<http://arxiv.org/ps/astro-ph/0209165v1>